

# Quantum Transport Characteristics of Lateral pn-Junction of Single Layer $\text{TiS}_3$

F. Iyikanat,<sup>1,\*</sup> R. T. Senger,<sup>1</sup> F. M. Peeters,<sup>2</sup> and H. Sahin<sup>3,†</sup>

<sup>1</sup>*Department of Physics, Izmir Institute of Technology, 35430, Izmir, Turkey*

<sup>2</sup>*Department of Physics, University of Antwerp, Groenenborgerlaan 171, 2020 Antwerp, Belgium*

<sup>3</sup>*Department of Photonics, Izmir Institute of Technology, 35430, Izmir, Turkey*

(Dated: October 11, 2016)

Using density functional theory and nonequilibrium Green's functions-based methods we investigated the electronic and transport properties of monolayer  $\text{TiS}_3$  pn-junction. We constructed a lateral pn-junction in monolayer  $\text{TiS}_3$  by using Li and F adatoms. An applied bias voltage caused significant variability in the electronic and transport properties of the  $\text{TiS}_3$  pn-junction. In addition, spin dependent current-voltage characteristics of the constructed  $\text{TiS}_3$  pn-junction were analyzed. Important device characteristics were found such as negative differential resistance and rectifying diode behaviors for spin-polarized currents in the  $\text{TiS}_3$  pn-junction. These prominent conduction properties of  $\text{TiS}_3$  pn-junction offer remarkable opportunities for the design of nanoelectronic devices based on a recently synthesized single-layered material.

## I. INTRODUCTION

In recent years, two-dimensional materials have attracted a lot of interest due to their wealth of potential applications in various fields. Among the large family of two-dimensional materials, transition metal dichalcogenides (TMDs) stick out due to their exceptional electronic and optical properties.<sup>1-3</sup> TMDs are van der Waals (vdW) stacked layered materials.<sup>4-6</sup> Many of the TMDs have been shown to undergo an indirect-to-direct band gap transition when exfoliated down to a monolayer.<sup>7,8</sup> Thus they are direct band gap semiconductor in the monolayer form. Due to the chemical versatility of this class of materials they exhibit a wide range of mechanical, electronic and optical characteristics.<sup>9-12</sup>

In addition to TMDs there is important class of materials that are stable in atomic layer form: transition metal trichalcogenides (TMTs). Similar to TMDs, TMTs also exhibit layered structures that are held together by weak vdW interactions. Most of the crystal structures of TMTs belong to the space group  $P2_1/m$  and they consist of one-dimensional chains of trigonal prisms with the metal atom occupying the center of each prism. Unlike the TMDs, single, few layer or even macroscopically thick TMTs may display direct-gap semiconducting behavior. Electronic and optical properties of various types of bulk TMTs such as  $\text{ZrSe}_3$ ,  $\text{HfSe}_3$ ,  $\text{TiS}_3$ ,  $\text{ZrS}_3$ ,  $\text{ZrTe}_3$  have been investigated experimentally.<sup>13-16</sup> Previous studies have shown that, bulk  $\text{TiS}_3$  is an n-type semiconductor with an energy band gap of 1 eV and it was shown that, it has a room temperature electronic mobility of about  $30 \text{ cm}^2 \text{ V}^{-1} \text{ s}^{-1}$ .<sup>17</sup> A nonlinear current-voltage characteristics of bulk  $\text{TiS}_3$  has been observed below 60 K.<sup>18</sup> Compared to TMDs, TMTs have drawn little attention until recently, which changed when the single layer  $\text{TiS}_3$  was isolated.<sup>19</sup>

The exfoliation of a single layer of titanium trisulfide ( $\text{TiS}_3$ ), has triggered tremendous interest in the electronic device community.<sup>19</sup> Recently Jin *et al.* theoretically studied structural, electronic and optical properties of titanium and zirconium trichalcogenide monolay-

ers and they found that monolayers of  $\text{TiTe}_3$  and  $\text{ZrTe}_3$  are metallic,  $\text{TiSe}_3$ ,  $\text{ZrSe}_3$ , and  $\text{ZrS}_3$  are indirect while  $\text{TiS}_3$  is a direct band gap semiconductor.<sup>22</sup> Moreover, they showed that these monolayer semiconductors exhibit anisotropic conductive properties. The effect of tensile strain on the electronic properties of monolayers of TMTs have been studied.<sup>20</sup> We have recently investigated structural and electronic properties of defective and oxidized monolayer  $\text{TiS}_3$ .<sup>21</sup> Previous experimental studies on monolayer  $\text{TiS}_3$  have revealed that it has a direct band gap of 1.10 eV and it exhibits a high carrier mobility in the few-layer limit.<sup>23,24</sup> Recently, novel field-effect transistors based on few-layer  $\text{TiS}_3$  were demonstrated.<sup>19,25</sup> Island *et al.* showed that, these transistors demonstrate promising device characteristics such as electron mobility of  $2.6 \text{ cm}^2 \text{ V}^{-1} \text{ s}^{-1}$  and n-type semiconducting behavior with ultrahigh photoreponse and fast switching times at room temperature.<sup>19</sup> Strain engineering has been identified as one of the most promising strategies to tune the band gap because the reduced-dimensional structures can sustain much larger strains than bulk crystals.<sup>26,27</sup> Strong nonlinearity of the current-voltage characteristics has been reported by Gorlova *et al.*<sup>28,29</sup> Especially, the nonlinearity in the current-voltage characteristics, the relatively high carrier mobility and the direct band gap properties even for a thickness of hundreds of layers make  $\text{TiS}_3$  a potential candidate for future electronics.

In the present study, structural, electronic, magnetic and transport properties of p- and n-doped  $\text{TiS}_3$  are investigated. The computational methodology is given in Sec. 2. Structural, electronic and magnetic properties of pristine, Li, and F doped monolayers of  $\text{TiS}_3$  are studied in Sec. 3 and 4. Transport properties of  $\text{TiS}_3$  pn-junction are investigated in Sec. 5. We summarize our results in Sec. 6.

## II. COMPUTATIONAL METHODOLOGY

All ionic and electronic relaxations are carried out within the framework of spin-polarized density functional theory (DFT) method implemented in the SIESTA package.<sup>32</sup> The Perdew-Burke-Ernzerhof generalized gradient approximation (PBE-GGA) is used for the exchange correlation functional. The Grimme's DFT-D2 dispersion correction is used to include the long-range vdW interactions.<sup>30,31</sup> A double- $\zeta$  polarized basis set is used and the mesh cutoff is chosen as 350 Ry. The convergence criterion for the energy is taken as  $10^{-5}$  eV. All atomic positions are fully relaxed with a force tolerance of 0.04 eV/Å. A vacuum space of at least 15 Å is used to prevent undesirable interactions between adjacent layers. Pressures on the unitcell are decreased to values less than 1.0 kBar. Structural calculations are performed with a  $7 \times 11 \times 1$  Monkhorst-Pack Grid. A k-point sampling of  $3 \times 3 \times 1$  is used for geometric calculations in  $3 \times 4 \times 1$  supercell. The Bader charge population analysis is performed to calculate the charge transfer between adatoms and  $\text{TiS}_3$ .<sup>35</sup>

The electronic transport calculations are performed by using the TRANSIESTA code, which is based on nonequilibrium Green's function formalism and DFT (NEGF-DFT).<sup>36</sup> The current through the central region is evaluated by the Landauer-Büttiker formula

$$I(V) = \frac{2e}{h} \int [f(E - \mu_L) - f(E - \mu_R)] T(E, V) dE, \quad (1)$$

where  $E$  denotes the energy,  $\mu_L$  and  $\mu_R$  are the electrochemical potentials of the left and right electrodes,  $V$  is the applied voltage,  $T(E, V)$  is the quantum mechanical transmission probability of electrons.  $e$ ,  $h$  and  $f$  denote electron charge, Planck's constant and Fermi function, respectively. Fully relaxed coordinates for the transport calculation, with a mesh cutoff of 350 Ry and a double- $\zeta$  polarized basis set are used. The Brillouin zone normal to the transport direction is sampled by a k-point mesh of  $16 \times 1 \times 1$ .

## III. STRUCTURAL AND ELECTRONIC PROPERTIES OF SINGLE LAYER $\text{TiS}_3$

The calculated lattice constants of monolayer  $\text{TiS}_3$  are  $a = 4.97$  Å and  $b = 3.40$  Å, which are compatible with the previous studies.<sup>22,27</sup> As seen in Fig. 1(a), atoms in  $\text{TiS}_3$  are arranged in a chain-like structure which consists of a prismatic trigonal structure with the metal atom located at the centre and chalcogen atoms located at the corners of the prism. The unit cell of  $\text{TiS}_3$  consists of two Ti atoms and six S atoms, which is shown in Fig. 1(a). To demonstrate more clearly the geometric structure of  $\text{TiS}_3$ , S atoms from different planes of  $\text{TiS}_3$  are illustrated with different labels. Fig. 1(b) presents a side view of  $\text{TiS}_3$ . As shown in this figure, S atoms located on the bottom plane of  $\text{TiS}_3$  are labeled as  $\text{S}_1$ , whereas S atoms

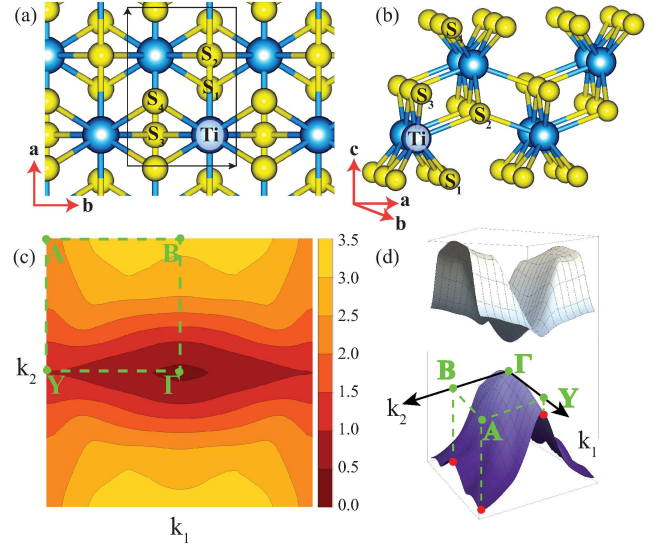


FIG. 1. (Color online) (a) Top view of monolayer  $\text{TiS}_3$  and its unit cell shown by a rectangle. For clarity, S atoms in the crystal are shown by yellow color and lowest layer S atom is presented as  $\text{S}_1$ , S atoms in the middle of the layer are shown by  $\text{S}_2$  and  $\text{S}_3$ , S atom in the top layer is illustrated by  $\text{S}_4$ . Ti atom in the crystal is shown by blue color and labelled by Ti. (b) Side view geometry of  $\text{TiS}_3$  along the  $a$  direction. (c) Contour plots of the band gap (in eV). (d) Tilted side view of the three-dimensional surface plots of valence and conduction bands.

placed on the top plane of  $\text{TiS}_3$  are labeled as  $\text{S}_4$ . These surface S atoms are bonded strongly to the Ti atoms with a bond length of 2.50 Å. Correspondingly, S atoms located in the middle of the  $\text{TiS}_3$  layer are denoted as  $\text{S}_2$  and  $\text{S}_3$ . The locations of  $\text{S}_2$  and  $\text{S}_3$  atoms in the structure are geometrically equivalent, and the bond lengths of the  $\text{S}_2$  and  $\text{S}_3$  atoms to the first and second nearest neighbour Ti atoms are 2.48 Å and 2.65 Å, respectively.

To investigate the electronic structure we performed a Bader analysis of the charge density as obtained from the SIESTA code. In a Bader charge analysis, atoms are defined by volumes bounded by surfaces of zero-flux. In these surfaces the gradient of the charge density is perpendicular to the normal vector of the surface. The integrated charges in the volume attributed to atoms are defined as Bader charge. In  $\text{TiS}_3$ , the bonds between inner-plane S atom ( $\text{S}_2$  or  $\text{S}_3$ ) and a Ti atom show ionic character with a charge transfer of 1.0  $e$  depleted from Ti atom to S atom. On the other hand, Ti atom donates 0.9  $e$  of valence charges to the two surface atoms (two  $\text{S}_1$  or two  $\text{S}_4$  atoms). These two surface S atoms share 0.9  $e$  and make a covalent bond with the Ti atom. As a result, in monolayer  $\text{TiS}_3$ , Ti atom has 2.1  $e$ ,  $\text{S}_2$  and  $\text{S}_3$  atoms possess 7.0  $e$  and  $\text{S}_1$  and  $\text{S}_4$  atoms have 6.45  $e$ .

Nanosheets and nanoribbons of  $\text{TiS}_3$  are used to fabricate FETs. While fabricated nanosheets exhibit high mobilities, nanoribbons exhibit higher optical response and gate tunability, but have lower mobility.<sup>19</sup> Previous

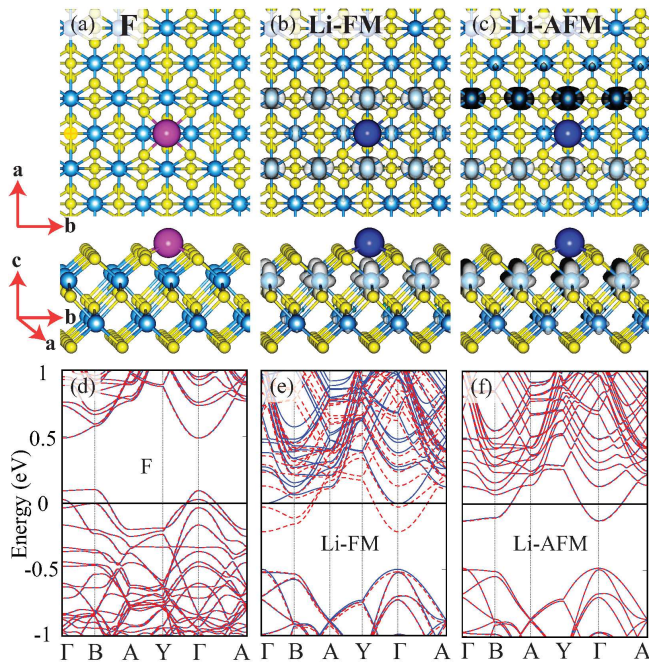


FIG. 2. (Color online) Top and side views of relaxed geometric structures and spin-dependent charge densities of TiS<sub>3</sub> are shown for F-doped layer (a), Li-doped layer in the ferromagnetic (Li-FM) (b), and antiferromagnetic (Li-AFM) (c) states. While white regions show majority spin charge densities, black regions show minority spin charge densities. Corresponding band structures of F-doped (d), Li-FM (e) and Li-AFM (f). Red dashed and blue solid lines show majority and minority spin bands, respectively.

experimental and theoretical studies have shown that, exceptional chain-like structure of TiS<sub>3</sub> leads to anisotropic conductive properties, i. e. the resistivity of TiS<sub>3</sub> across the chains are significantly higher than the resistivity along the chains.<sup>15,22</sup> In order to properly understand the electronic properties of TiS<sub>3</sub>, contours plots of band gap energies in reciprocal space of TiS<sub>3</sub> are depicted in Fig. 1(c). Monolayer TiS<sub>3</sub> is a direct-gap semiconductor with a band gap of 1.10 eV.<sup>20–22</sup> Our PBE calculated band gap value of TiS<sub>3</sub> is 0.45 eV. It is well known that the bare PBE underestimates the band gap values of semiconductors. However, the electronic band dispersion is well-approximated by PBE. As seen from Fig. 1(c), TiS<sub>3</sub> has a direct band gap with both the valence-band-maximum (VBM) and the conduction-band-minimum (CBM) residing at the  $\Gamma$  point, and variation of the gap along the  $\Gamma$ -Y direction is small. VB and CB give quite valuable information about the electronic structure of a material. Three-dimensional surface plots of VB and CB of TiS<sub>3</sub> are shown in Fig. 1(d). The plotted surfaces clearly show that VB and CB surfaces are highly anisotropic. The electron mobility along  $k_2$  direction is much larger than that along the perpendicular direction. This makes it clear that the contribution to the electronic conductivity parallel to the chain direction will be much larger

than that corresponding to normal to the chain direction.

#### IV. P- AND N- TYPE DOPING OF TiS<sub>3</sub>

Top and side views of the relaxed geometric structure of F-doped TiS<sub>3</sub> are shown in Fig. 2(a). Li-doped TiS<sub>3</sub> has magnetically two different states which are denoted as Li-FM and Li-AFM and shown in Figs. 2(b) and (c), respectively. The structural and electronic properties of these states are given in Table I. As shown in Figs. 2(a)-(c), both adatoms are placed in the middle of the four S atoms. While Li atom binds at a distance 0.86 Å, F atom is located 0.79 Å above the surface. In order to hinder the interactions between the adatoms of adjacent supercells, a  $3 \times 4 \times 1$  supercell is used for electronic structure calculations. Both Li and F atoms do not cause any significant structural deformation, thus TiS<sub>3</sub> preserves its lattice constant values, which are in the supercell form  $a = 14.90$  and  $b = 13.61$  Å. The binding energies are calculated using the expression  $E_{bind} = E_{TiS_3+Adatom} - E_{TiS_3} - E_{Adatom}$ , where  $E_{bind}$  is the binding energy of the considered adatom,  $E_{TiS_3+Adatom}$  is the energy of adatom doped TiS<sub>3</sub>,  $E_{TiS_3}$  is the energy of pristine TiS<sub>3</sub> and  $E_{Adatom}$  is the energy of the considered adatom. As listed in Table I, binding energies of F, Li-FM, and Li-AFM on TiS<sub>3</sub> are calculated to be 2.48 and 2.98, and 2.99 eV, respectively.

TABLE I. Perpendicular distance of the adatom from the surface of the layer,  $h$ . The preferred binding site, where the hollow site is denoted by H. The binding energy of adatom,  $E_{bind}$ . Bader charge transferred from adatom to TiS<sub>3</sub>,  $\Delta\rho$ . Magnetic moment per supercell,  $\mu$ .

	$h$ (Å)	Binding Site	$E_{bind}$ (eV)	$\Delta\rho$ (e)	$\mu$ ( $\mu_B$ )
F	0.79	H	2.48	-0.6	0.0
Li-FM	0.86	H	2.98	+1.0	0.9
Li-AFM	0.86	H	2.99	+1.0	0.0

Bader charge analysis shows that F adatom gains 0.6  $e$  when it is placed on TiS<sub>3</sub>. Contrary to F, Li adatom donates all its valence charge (1  $e$ ) to TiS<sub>3</sub>. The non-magnetic nature of the monolayer TiS<sub>3</sub> is not affected by F doping. However, Li doping significantly changes the magnetic properties of TiS<sub>3</sub> and two different magnetic states are generated. One of them is denoted as Li-FM state, and the other is denoted as Li-AFM state and as given in Table I their magnetic moment values are 0.9 and 0.0  $\mu_B$  per supercells. Our results show that Li-FM is the ground state. However, calculated energy difference between Li-FM and Li-AFM states is only 5 meV. Thus, Li-AFM state can not be ignored and both of the states are considered in the present paper. Spin polarized charge densities of Li-doped TiS<sub>3</sub> for FM and AFM states are shown from top and side views in Figs. 2(b) and (c), respectively. As seen in the figure of Li-FM, Ti atoms of the nearest two chains to the Li adatom are polarized



ferromagnetically. While the nearest Ti atom to the Li adatom has a magnetic moment of  $0.21 \mu_B$ , this value decreases to  $0.14 \mu_B$  for the furthest Ti atom. On the other hand, Fig 2(c) shows that Ti atoms of the nearest two chains to the Li adatom are polarized antiferromagnetically. As in the case of Li-FM, magnetic moments of individual Ti atoms are decreasing when the distance to the Li adatom is increased. Absolute values of magnetic moment of individual Ti atoms are almost the same in the Li-FM and Li-AFM states. However, in both cases S atoms do not exhibit any significant magnetic moment.

In order to investigate the effect of adatom doping on the electronic structure of  $\text{TiS}_3$ , band diagrams of F- and Li-doped  $3 \times 4 \times 1$   $\text{TiS}_3$  are calculated and showed in Figs. 2(d)-(f). As mentioned above Li-doped  $\text{TiS}_3$  has two different magnetic states with very similar energy values and their band diagrams are also shown in these figures. Fig. 2(d) shows that, when  $\text{TiS}_3$  is doped with F atoms, some states of  $\text{TiS}_3$  discharge because F atom receive  $0.6 e^-$  from it. Thus, F doping results in acceptor states close to the top of the valence band. These results suggest that F doping causes p-type doping of  $\text{TiS}_3$ . Flat bands of F atoms appear  $\sim 0.3$  eV below the Fermi level. On the other hand, donor states occur close to the conduction band minimum when  $\text{TiS}_3$  is doped with Li atoms. Fig. 2(e) shows that, the donor states come from only the majority spin component in the Li-FM state. However, as shown in Fig. 2(f), in the Li-AFM state all bands are degenerate and the donor states originate from charges with both spin components. Adsorption of Li atoms on  $\text{TiS}_3$  leads to n-type doping. Created donor and acceptor states are necessary for the construction of a pn-junction. Thus, doping one side of a  $\text{TiS}_3$  layer with F (a p-type dopant) and the other side with Li (an n-type dopant) forms a pn-junction. One can modulate the electronic properties of  $\text{TiS}_3$  by changing the atom type of the dopant and the doping concentrations.

## V. TRANSPORT PROPERTIES OF $\text{TiS}_3$ PN-JUNCTION

A pn-junction can be constructed by combining p-type and n-type materials in lateral or vertical orientation. Because of the controllability of its electronic properties and its possible applications, pn-junctions are used in many semiconductor devices. To construct a pn-junction, the presence of shallow p- and n-type doping levels are essential. In the previous part, we have shown that, p- and n-type doping of  $\text{TiS}_3$  can be realized through doping with F and Li atoms, respectively. Thus when we construct a device which consist of p-type and n-type doped parts of  $\text{TiS}_3$ , states near the valence and conduction bands will behave like acceptor and donor states. The quantum transport properties of a monolayer  $\text{TiS}_3$ -based pn-junction are investigated in the following.

The device setup used for the transport calculations on the  $\text{TiS}_3$  pn-junction is shown in Fig. 3. The device

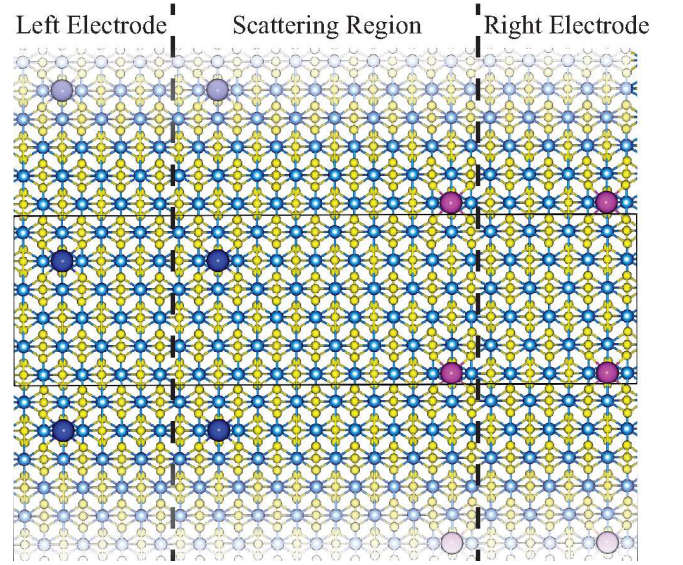


FIG. 3. (Color online) Li and F doped device structure of  $\text{TiS}_3$  pn-junction. Blue and purple atoms illustrate Li and F atoms, respectively.

geometry consists of semi-infinite left electrode, semi-infinite right electrode, and a scattering region. The possibility of experimental realization of  $\text{TiS}_3$  pn-junction is highly dependent on the dopant atom concentrations. Thus, to simulate the electrode parts of the device, one adatom of Li or F and a  $3 \times 1 \times 4$  supercell of  $\text{TiS}_3$  are used. In the present study, ground state of Li-FM is used for the transport calculations of  $\text{TiS}_3$  pn-junction. The adatom concentration is the same  $\sim 5 \times 10^{13} \text{ cm}^{-2}$  for both electrodes. The distance between Li and F atoms in the scattering region is taken to be  $22.7 \text{ \AA}$ . Recent studies have shown that, monolayer  $\text{TiS}_3$  exhibits conductance anisotropy, and the electron mobility along the chain direction is larger than across the chain direction.<sup>15,22</sup> Therefore, the transport direction of the device geometry is chosen to be the chain direction.

Fig. 4 presents transmission profiles per unit length of constructed  $\text{TiS}_3$  pn-junction for varying bias voltages. As shown in Fig. 4(c), in the unbiased situation  $\text{TiS}_3$  pn-junction has a transport gap of  $0.99 \text{ eV}$ . VBM and CBM of this transport gap coincides with the VBM of Li doped  $\text{TiS}_3$  and CBM of F doped  $\text{TiS}_3$ , respectively. Inset of Fig. 4(c) shows transmission profile of  $\text{TiS}_3$  pn-junction zoomed around the Fermi level, which is shown by dashed rectangle. These small transmissions occur when the valence band states of F doped region overlap with the conduction band states of Li doped region. Therefore, charges from valence band of the F doped source region can tunnel to the empty conduction band of Li doped region. As shown in Figs. 4 (a)-(f), applying bias voltage leads to significant modulation in the electronic properties of  $\text{TiS}_3$  pn-junction.

First of all, increasing bias voltage of pn-junction shifts the energy bands of F doped electrode to the lower energy

values, whereas it shifts the energy bands of Li doped electrode to higher energy values. As a result, when the bias voltage is increased from -0.2 V to 0.3 V, the transport gap of the  $\text{TiS}_3$  pn-junction decreases from 1.19 eV to 0.68 eV.

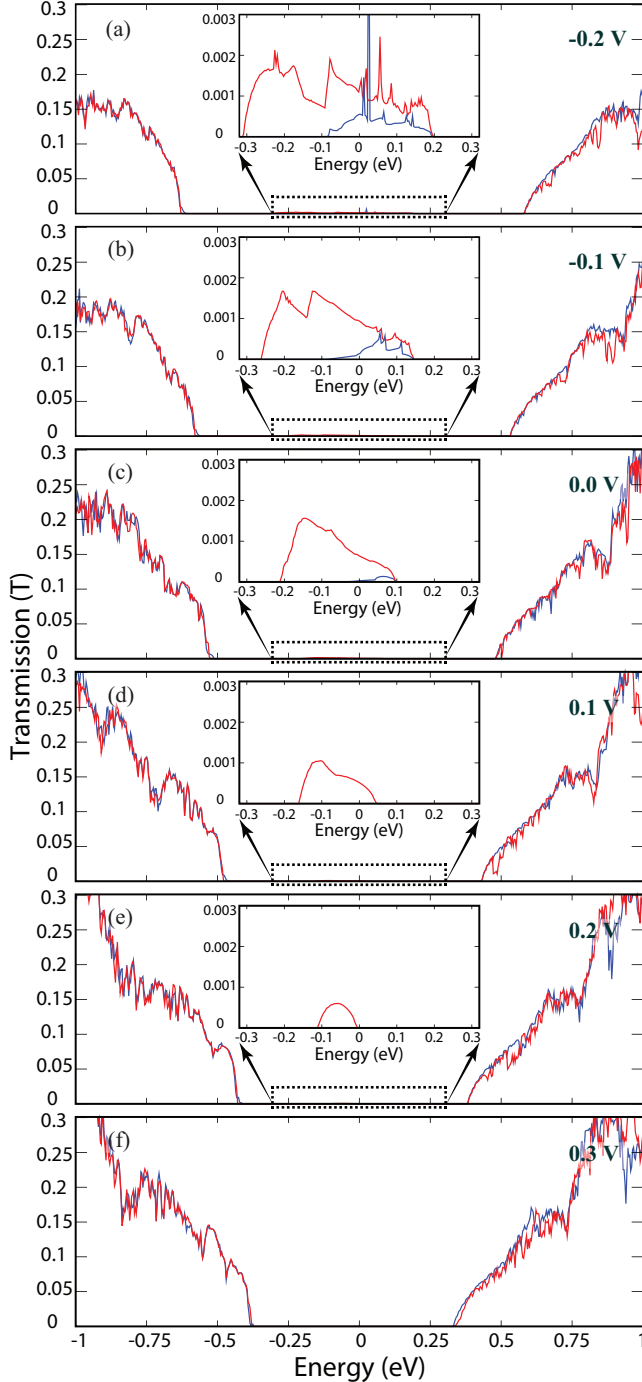


FIG. 4. (Color online) Transmission of  $\text{TiS}_3$  pn-junction for different bias. Insets are zoomed transmissions in the vicinity of Fermi level. Transmission near the Fermi level completely diminish for bias of 0.3 V. Red and blue lines show majority and minority spin components of the transmission profiles, respectively.

Secondly, while transmission values near to the VBM and CBM look similar, for high energy values such as -1.0 eV, transmission values are increasing from 0.15 to 0.30 with increasing bias voltage from -0.2 V to 0.3 V. As can be seen from Fig. 2, near to the edges of the CBM of F doped  $\text{TiS}_3$  and the VBM of Li doped  $\text{TiS}_3$  consist of a smaller number of bands relative to the deeper energies. When bias voltage is increased, deeper states of p-type doped and n-type doped parts of the  $\text{TiS}_3$  contribute to the transmission. Thus, rising of the transmission values of  $\text{TiS}_3$  pn-junction to high energy ranges can be expressed by the shifting of deeper states of the left and right electrodes. On the other hand, spin-up and spin-down transmission profiles are almost the same for the considered energy range and bias values.

Lastly, Fig. 4 shows that, transmission in the vicinity of the Fermi level is decreasing with increasing bias voltage from -0.2 to 0.3 V. Due to quantum tunnelling between the electrodes, there is only small transmission between energy values of -0.2 and 0.1 eV, even in the unbiased situation, which is shown in the inset of Fig. 4(c). In the previous part, we showed that Li doped  $\text{TiS}_3$  is magnetic. Ti atoms near to the adsorbed atom possess a net magnetic moment with the same spin polarization. Therefore, transmission values of  $\text{TiS}_3$  pn-junction near the Fermi level are highly spin-polarized. Figs. 4(d)-(f) show that, with increasing bias voltage, the transmission near the Fermi level decreases and at 0.3 V bias it is completely suppressed. On the other hand, when the bias voltage is increased in the other direction, energy range with the nonzero transmission and transmission values near the Fermi level increases for both spin components. Moreover, some small resonant states occur for applied bias voltage of -0.2 V, which is shown in the inset of Fig. 4(a).

The spin-up and spin-down  $I$ - $V$  characteristics of  $\text{TiS}_3$  pn-junction are shown in Fig. 5 by the red and blue curves, respectively. The corresponding current values are calculated for a scattering region of size 14.91 Å. Fig. 5 explicitly shows that, spin-up and spin-down  $I$ - $V$  characteristics of  $\text{TiS}_3$  pn-junction are rather different. Also this figure clearly shows that spin-up current exhibits negative differential resistance (NDR), when positive bias applied to the system. Spin-up and spin-down current show typical diode behavior for negative bias. The NDR phenomenon in this system can be explained by the variation of transmissions and the relative shifts of energy states of device and electrode regions with applied bias voltage. As shown in Figs. 4(c)-(e), small spin-up transmission peaks near the Fermi level are visible for  $0.0 \leq V < 0.3$ , and these transmission peaks disappear for bias voltage 0.3 V, whereas spin-down transmissions are zero for these positive bias voltage values. These small spin-up transmission peaks lead to negative differential resistance (NDR) between 0.0 V and 0.3 V in the spin-up  $I$ - $V$  characteristic of  $\text{TiS}_3$  pn-junction, as shown in Fig. 5. However, the spin-down current is zero for the positive bias voltage. On the other hand, when negative

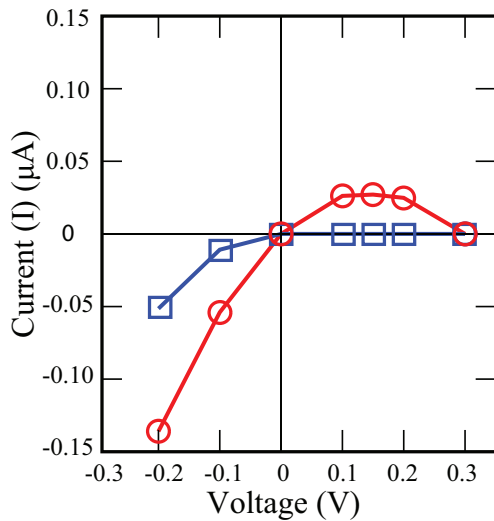


FIG. 5. (Color online) The calculated spin-up (red curve) and spin-down (blue curve) current-voltage ( $I$ - $V$ ) characteristics for  $\text{TiS}_3$  pn-junction.

bias voltage is applied, spin-up and spin-down transmission peaks occur near the Fermi level, with the dominant one being spin-up, as shown in Figs. 4(a), (b). As a result, the spin-up electrons flow more easily from the valence band of the F-doped electrode to the conduction band of the Li-doped electrode, than the spin-down electrons. This explains the higher spin-up current values of the  $\text{TiS}_3$  pn-junction for negative bias. Moreover, spin-up and spin-down transmission peaks near the Fermi level rise with increasing negative bias voltage. This leads to an increase in the spin-up and spin-down current values for higher negative bias voltages. As a result, the  $I$ - $V$  characteristic of a  $\text{TiS}_3$  pn-junction is strongly related to

the doping types, its effect on the magnetism and the amount of doping of the electrodes and scattering parts. While one spin component of the current shows NDR, both spin components of the current show a typical diode character.

## VI. CONCLUSIONS

In summary, we investigated electronic and transport properties of monolayer  $\text{TiS}_3$  pn-junction by using density functional theory and nonequilibrium Green's functions method. Doping one side of a  $\text{TiS}_3$  layer with F adatom (a p-type dopant) and the other side with Li adatom (an n-type dopant) forms a lateral pn-junction. We showed that the conduction properties of  $\text{TiS}_3$  pn-junction can be tuned by applying a bias voltage. The predicted device showed NDR behavior only for one spin component of the current. Both spin components of the current had asymmetric characteristics with respect to the bias voltage, thus, they showed rectifying diode behavior. Prediction of a pn-junction based on monolayer  $\text{TiS}_3$  reveals a functional application of this new material.

## VII. ACKNOWLEDGMENTS

This work was supported by the bilateral project between TUBITAK (through Grant No. 113T050) and the Flemish Science Foundation (FWO-VI). The calculations were performed at TUBITAK ULAKBIM, High Performance and Grid Computing Center (TR-Grid e-Infrastructure). FI, HS, and RTS acknowledge the support from TUBITAK Project No 114F397. H.S. acknowledges support from Bilim Akademisi-The Science Academy, Turkey under the BAGEP program.

\* fadiliyikanat@iyte.edu.tr

† hasansahin@iyte.edu.tr

<sup>1</sup> K. S. Novoselov, D. Jiang, F. Schedin, T. J. Booth, V. V. Khotkevich, S. V. Morozov, and A. K. Geim, *Proc. Natl. Acad. Sci. USA* **2005**, 102, 10451-10453.

<sup>2</sup> Q. H. Wang, K. K.-Zadeh, A. Kis, J. N. Coleman, and M. S. Strano, *Nat. Nanotechnol.* **2012**, 7, 699-712.

<sup>3</sup> M. Chhowalla, H. S. Shin, G. Eda, L. -J. Li, K. P. Loh, and H. Zhang, *Nat. Chem.* **2013**, 5, 263-275.

<sup>4</sup> Y. Zhao, X. Luo, H. Li, J. Zhang, P. T. Araujo, C. K. Gan, J. Wu, H. Zhang, S. Y. Quek, M. S. Dresselhaus, and Q. Xiong, *Nano Lett.* **2013**, 13, 1007-1015.

<sup>5</sup> A. K. Geim and I. V. Grigorieva, *Nature* **2013**, 499, 419-425.

<sup>6</sup> G. Cunningham, M. Lotya, C. S. Cucinotta, S. Sanvito, S. D. Bergin, R. Menzel, M. S. P. Shaffer, and J. N. Coleman, *ACS Nano* **2012**, 6, 3468-3480.

<sup>7</sup> K. F. Mak, C. Lee, J. Hone, J. Shan, and T. F. Heinz, *Phys. Rev. Lett.* **2010**, 105, 136805.

<sup>8</sup> W. Zhao, Z. Ghorannevis, L. Chu, M. Toh, C. Kloc, P. -H. Tan, and G. Eda, *ACS Nano* **2013**, 7, 791-797.

<sup>9</sup> D. Jariwala, V. K. Sangwan, L. J. Lauhon, T. J. Marks, and M. C. Hersam, *ACS Nano* **2014**, 8, 1102-1120.

<sup>10</sup> A. Splendiani, L. Sun, Y. Zhang, T. Li, J. Kim, C. -Y. Chim, G. Galli, and F. Wang, *Nano Lett.* **2010**, 10, 1271-1275.

<sup>11</sup> S. Manzeli, A. Allain, A. Ghadimi, and A. Kis, *Nano Lett.* **2015**, 15, 5330-5335.

<sup>12</sup> R. M. Elder, M. R. Neupane, and T. L. Chantawansri, *App. Phys. Lett.* **2015**, 107, 073101.

<sup>13</sup> M. Hoesch, X. Cui, K. Shimada, C. Battaglia, S. -i. Fujimori, and H. Berger, *Phys. Rev. B* **2009**, 80, 075423.

<sup>14</sup> D. Pacilé, M. Papagno, M. Lavagnini, H. Berger, L. Degiorgi, and M. Grioni, *Phys. Rev. B* **2007**, 76, 155406.

<sup>15</sup> I. G. Gorlova, V. Y. Pokrovskii, S. G. Zybtsev, A. N. Titov, and V. N. Timofeev, *JETP* **2010**, 111, 298-303.

<sup>16</sup> E. Guilmeau, D. Berthebaud, P. R. N. Misse, S. Hébert, O. I. Lebedev, D. Chateigner, C. Martin, and A. Maignan, *Chem. Mater.* **2014**, 26, 5585-5591.

- <sup>17</sup> E. Finkman and B. Fisher, Solid State Commun. **1984**, 50, 25-28.
- <sup>18</sup> I. G. Gorlova and V. Y. Pokrovskii, JETP Lett. **2009**, 90, 295.
- <sup>19</sup> J. O. Island, M. Barawi, R. Biele, A. Almazán, J. M. Clamagirand, J. R. Ares, C. Sánchez, H. S. J. van der Zant, J. V. Álvarez, R. D'Agosta, I. J. Ferrer, and A. Castellanoz-Gomez, Adv. Mater. **2015**, 27, 2595-2601.
- <sup>20</sup> M. Li, J. Dai, and X. C. Zeng, Nanoscale **2015**, 7, 15385-15391.
- <sup>21</sup> F. Iyikanat, H. Sahin, R. T. Senger, and F. M. Peeters, J. Phys. Chem. C **2015**, 119, 10709-10715.
- <sup>22</sup> Y. Jin, X. Li, and J. Yang, Phys. Chem. Chem. Phys. **2015**, 17, 18665-18669.
- <sup>23</sup> I. J. Ferrer, J. R. Ares, J. M. Clamagirand, M. Barawi, and C. Sanchez, Thin Solid Films **2012**, 535, 398-401.
- <sup>24</sup> I. J. Ferrer, M. D. Marciá, V. Carcelén, J. R. Ares, and C. Sanchez, Energy Procedia **2012**, 22, 48-52.
- <sup>25</sup> A. Lipatov, P. M. Wilson, M. Shekhirev, J. D. Teeter, R. Netusil, and A. Sinitskii, Nanoscale **2015**, 7, 12291-12296.
- <sup>26</sup> J. Kang, H. Sahin, H. D. Sengun, R. T. Senger, and F. M. Peeters, Phys. Rev. B **2015**, 92, 075413.
- <sup>27</sup> J. Kang, H. Sahin, and F. M. Peeters, Phys. Chem. Chem. Phys. **2015**, 17, 27742-27749.
- <sup>28</sup> I. Gorlova, S. Zybtssev, V. Y. Pokrovskii, N. Bolotina, I. Verin, A. Titov, Physica B **2012**, 407, 1707-1710.
- <sup>29</sup> I. G. Gorlova, S. G. Zybtssev, and V. Y. Pokrovskii, JETP Letters **2014**, 100, 256.
- <sup>30</sup> J. P. Perdew, K. Burke, and M. Ernzerhof, Phys. Rev. Lett. **1996**, 77, 3865.
- <sup>31</sup> S. Grimme, J. Comp. Chem. **2006**, 27, 1787-1799.
- <sup>32</sup> J. M. Soler, E. Artacho, J. D. Gale, A. García, J. Junquera, P. Ordejón, and D. Sánchez-Portal, J. Phys.: Condens. Matter **2002**, 14, 2745-2779.
- <sup>33</sup> J. O. Island, M. Buscema, M. Barawi, J. M. Clamagirand, J. R. Ares, C. Sánchez, I. J. Ferrer, G. A. Steele, H. S. van der Zant and A. Castellanos-Gomez, Adv. Opt. Mater. **2014**, 2, 641-645.
- <sup>34</sup> M. Barawi, E. Flores, I. J. Ferrer, J. R. Ares, C. Sánchez, J. Mater. Chem. A **2015**, 3, 7959-7965.
- <sup>35</sup> G. Henkelman, A. Arnaldsson, and H. Jonsson, Comp. Mat. Sci. **2006**, 36, 354-360.
- <sup>36</sup> M. Brandbyge, J.-L. Mozos, P. Ordejón, J. Taylor, and K. Stokbro, Phys. Rev. B **2002**, 65, 165401.
- <sup>37</sup> L. Brattas and A. Kjekshus, Acta Chem. Scand. **1972**, 26, 3441-3449.
- <sup>38</sup> S. Furuseth, L. Brattas, and A. Kjekshus, Acta Chem. Scand. A **1975**, 29, 623-631.